



## UvA-DARE (Digital Academic Repository)

### Chain oscillations in liquid jets

Jordan, D.T.A.; Ribe, N.M.; Deblais, A.; Bonn, D.

**DOI**

[10.1103/PhysRevFluids.7.104001](https://doi.org/10.1103/PhysRevFluids.7.104001)

**Publication date**

2022

**Document Version**

Final published version

**Published in**

Physical Review Fluids

[Link to publication](#)

**Citation for published version (APA):**

Jordan, D. T. A., Ribe, N. M., Deblais, A., & Bonn, D. (2022). Chain oscillations in liquid jets. *Physical Review Fluids*, 7(10), [104001]. <https://doi.org/10.1103/PhysRevFluids.7.104001>





**General rights**

It is not permitted to download or to forward/distribute the text or part of it without the consent of the author(s) and/or copyright holder(s), other than for strictly personal, individual use, unless the work is under an open content license (like Creative Commons).

**Disclaimer/Complaints regulations**

If you believe that digital publication of certain material infringes any of your rights or (privacy) interests, please let the Library know, stating your reasons. In case of a legitimate complaint, the Library will make the material inaccessible and/or remove it from the website. Please Ask the Library: <https://uba.uva.nl/en/contact>, or a letter to: Library of the University of Amsterdam, Secretariat, Singel 425, 1012 WP Amsterdam, The Netherlands. You will be contacted as soon as possible.

## Chain oscillations in liquid jets

Daniel T. A. Jordan <sup>1,\*</sup> Neil M. Ribe <sup>2,†</sup> Antoine Deblais <sup>1</sup> and Daniel Bonn <sup>1,‡</sup>

<sup>1</sup>*Van der Waals-Zeeman Institute, IOP, University of Amsterdam, Science Park 904,  
1098 XH Amsterdam, Netherlands*

<sup>2</sup>*Lab FAST, Université Paris-Saclay, CNRS, 91405 Orsay, France*



(Received 15 June 2022; accepted 1 September 2022; published 11 October 2022)

A circular jet breaks up into droplets via the Rayleigh-Plateau instability, retaining a circular cross section throughout. If, however, the nozzle from which the jet issues is elongated, the circular symmetry is broken, and the jet forms a chainlike structure with neighboring links separated by  $90^\circ$ . The cause of this structure is two-dimensional capillary-inertial oscillation of jet cross sections in their own plane. We perform an experimental study of chain oscillations as a function of flow rate using careful prelamination and 12 elliptical nozzles with different areas and eccentricities. The oscillation frequencies inferred from the observed chain-link structure do not agree with those predicted by Rayleigh's infinitesimal theory [L. Rayleigh, Proc. R. Soc. London **29A**, 71 (1879)]. However, they do agree with an extended nonlinear theory of Bohr [N. Bohr, *Philos. Trans. R. Soc. A* **209**, 281 (1909)] that accounts for finite-amplitude effects. This agreement shows that our fluid chains are nonlinear oscillations whose frequency decreases with increasing amplitude. We perform direct numerical simulations of chain oscillations using a volume-of-fluid method and find good agreement with the predictions of Bohr's theory. Finally, we generalize Bohr's theory to the case of two interacting modes with quadrupolar and octapolar azimuthal dependencies. The resulting solution explains qualitatively the "dimpled" shape of the jet's surface observed in the experiments.

DOI: [10.1103/PhysRevFluids.7.104001](https://doi.org/10.1103/PhysRevFluids.7.104001)

### I. INTRODUCTION

Anyone who has observed water poured from a glass has seen the surprising "liquid chain" effect, in which a steady liquid stream exhibits a series of "links" oriented at  $90^\circ$  to one another (see Fig. 1). The effect is also observable in a liquid jet falling from a nozzle with an elliptical or other noncircular cross section, in which case several links are typically observed before the jet breaks up. Because the long and short axes of the jet exchange places periodically as a function of distance along with the jet, the phenomenon is also called "axis switching." Despite its generic character, the liquid chain or axis switching phenomenon remains incompletely understood.

For more than a century, axisymmetric jets with circular cross sections have been intensively studied owing to the importance of the Rayleigh-Plateau (RP) instability [1]. This surface-tension-driven instability leads to the breakup of a liquid jet in response to axisymmetric perturbations of its surface. However, Rayleigh [2] also examined nonaxisymmetric perturbations of the surface of a jet and found that these took the form of stable oscillations with frequencies that increased with the azimuthal wavenumber  $n$ . It is these stable oscillations that underlie the liquid chain effect.

\*These two authors contributed equally.

†[ribe@fast.u-psud.fr](mailto:ribe@fast.u-psud.fr)

‡[d.bonn@uva.nl](mailto:d.bonn@uva.nl)



FIG. 1. Pouring water from a bottle. (a) Chain oscillations are excited because the initial cross section is noncircular, as highlighted by the dashed line.

The liquid chain effect seems first to have been studied experimentally by Bidone [3], who noted that the wavelength  $\lambda$  of the axis switching was an increasing function of the jet speed  $W$ . According to Rayleigh [2], the first correct explanation of axis switching was given by Buff [4], who ascribed it to transverse vibrations of jet cross sections about a circular equilibrium shape under the action of surface tension. Because the phase of the oscillation depends on the time elapsed since ejection from the nozzle, the structure of the jet is steady in the laboratory frame. Rayleigh [2] performed experiments on chain oscillations using orifices of different shapes and found that  $\lambda \propto W$  under most conditions. He speculated that departures from this linear dependence were due to the finite amplitude of the oscillations. Bohr [5] extended Rayleigh's linearized theory into the finite-amplitude regime, obtaining expressions for the jet's shape and its frequencies of oscillation valid to second order in the amplitude.

More than 70 years later, Geer and Strikwerda [6] used a numerical method to simulate axis switching in an inviscid jet without restriction on the amplitude of the oscillations. Bechtel [7] used an analytical slender-jet theory to model axis switching, assuming that the section is always elliptical. Neither Geer and Strikwerda [6] nor Bechtel [7] appear to have been aware of the work of Bohr [5]. Kasyap *et al.* [8,9] performed experiments using different elliptical orifices and characterized the chain wavelength and the oscillation amplitude systematically as functions of the jet speed and the distance from the nozzle. Amini and Dolatabadi [10] performed a spatial linear stability analysis of one-dimensional Cosserat-type equations for jets of elliptical cross section and proposed that the axis-switching wavelength is

$$\frac{\lambda}{R_{\text{eq}}} = \frac{2\pi}{\sqrt{6}} \sqrt{\text{We} - 2}, \quad (1)$$

where  $\text{We} = \rho R_{\text{eq}} W^2 / \gamma$  is the Weber number,  $R_{\text{eq}}$  is the equivalent radius of the cross section, and  $\gamma$  is the coefficient of surface tension. A similar Cosserat model was investigated by Gu *et al.* [11],

focusing on the effect of viscosity. Direct numerical simulations of axis switching were performed by Farvardin and Dolatabadi [12] and Morad *et al.* [13] using volume-of-fluid methods and by Chen and Yu [14] using a lattice Boltzmann method. Muthukumaran and Vaidyanathan [15] carried out experiments on elliptical jets under sub- and supercritical pressure and temperature conditions and obtained axis-switching wavelengths about 50% higher than Eq. (1). Rajesh *et al.* [16] performed experiments using nozzles of different shapes and found  $\lambda \propto R_{\text{eq}} We^{1/2}$  with an additional weak dependence on the downstream distance. Moon *et al.* [17] performed experiments using ethanol and water jets ejected from microscale (mean radius 11–15  $\mu\text{m}$ ) quasielliptical nozzles at a fixed exit velocity and used two different optical techniques to reconstruct the jet's surface shape. They found that the amplitude of the octapolar (azimuthal dependence  $\cos 4\theta$ ) component of the jet's shape relative to the quadrupolar ( $\cos 2\theta$ ) component agreed closely with Bohr's nonlinear theory. Jaber and Tadjfar [18, 19] used laboratory experiments to compare axis switching with elliptical and square nozzles. Ma and Zhu [20] performed experiments on axis switching in elliptical jets and proposed a way to correct the switching frequency for the effect of gravity. Finally, this is an appropriate place to mention the work of Bush and Hasha [21] on fluid chains formed by the collision of viscous laminar jets.

In addition to its fundamental interest, the dynamics of jets from noncircular nozzles have numerous practical applications. These include improving large- and small-scale mixing, enhancing combustion efficiency, noise suppression, and thrust vector control. A valuable survey of these applications is [22]. A further surprising application is in the field of urology [23].

In this study we extend existing work on chain oscillations in several ways. First, we perform systematic experiments for different flow rates and different aspect ratios of the (elliptical) nozzle, using a technique to prelaminarize the flow before it exits the nozzle. This gives rise to very smooth jets that exhibit numerous chain links before they break up  $\approx 1$  m from the nozzle. Second, we systematically compare our measured axis-switching frequencies with both the linear theory of Rayleigh [2] and the nonlinear theory of Bohr [5]. To our knowledge such a comparison has only been done previously by Moon *et al.* [17]. Finally, we extend Bohr's nonlinear solution to the case of two interacting modes  $n = 2$  and  $n = 4$ , a situation that is relevant for both elliptical and rectangular nozzles.

## II. PHENOMENOLOGY

Chain oscillations are most readily observed when the viscosities of the jet and the ambient fluid are low and the interface has a high surface tension. Water jets in air satisfy these criteria, and so it is no surprise that chain oscillations occur in many everyday situations. Deformation and vibration of a jet are capillary phenomena in which surface tension acts to reduce the jet's surface area. If the cross section is not circular, its highly curved portions are pulled inward and its weakly curved portions pushed outward relative to a circular section with the same area. But due to inertia the movement overshoots, with the result that the long and short axes of the section are interchanged. The shape of the section therefore evolves as it moves along the axis of the jet, producing a steady liquid chain when observed in the laboratory frame (see Fig. 2). The length  $l_{\text{link}}$  of a link is then just  $\lambda/2$  where  $\lambda$  is the wavelength of the pattern. Here, we investigate these chain oscillations experimentally and explain them theoretically by studying the normal modes of vibration of a capillary jet.

## III. RAYLEIGH THEORY

The radius  $R(\phi, z)$  of a perturbed cylindrical jet can be expanded in normal modes as

$$R(\theta, t) = a + \sum_{n=2}^{\infty} b_n \cos n\theta \cos \omega_n t, \quad (2)$$

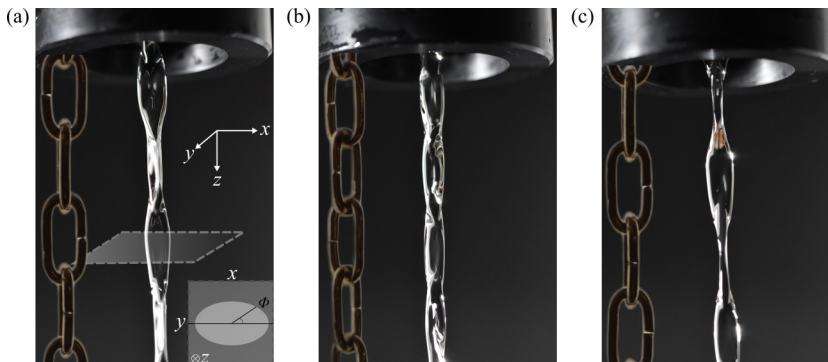


FIG. 2. Geometry of liquid and metal chains. The images shown are separated by rotations of  $45^\circ$  about the vertical axis. The inset in (a) sketches a cross section of the jet at a given height  $z$  and shows the polar coordinates.

where  $a$  is the unperturbed radius (in the limit of small perturbations), and  $\omega_n$  and  $b_n$  are the angular frequency and amplitude of mode  $n$ , respectively. The time

$$t = \int_0^z \frac{dz}{W(z)} \quad (3)$$

is just the travel time of a fluid cross section from the nozzle  $z = 0$  to a position  $z$ , where  $W(z)$  is the vertical velocity of the section. If the perturbations become larger and if only one mode is present, then

$$R(\theta, t) = a - \frac{b^2}{8a} + b \cos n\theta \cos \omega_n t, \quad (4)$$

where the additional term  $-b^2/8a$  ensures that the area of the cross section is  $A = \pi a^2$  (it should be replaced by  $-b^2/4a$  if  $n = 0$ ). This term can be neglected in the small-amplitude limit  $b \ll a$ .

The modes in Eq. (2) include the unstable axisymmetric mode  $n = 0$  corresponding to the Rayleigh-Plateau instability and the nonaxisymmetric modes  $n \geq 2$  that are, in theory, stable. In practice, of course, the unstable axisymmetric mode will be superimposed on the stable modes, leading to the breakup of the jet all the same. If the axial velocity  $W$  of the jet is constant, the motion associated with the stable modes is a purely two-dimensional (2D) oscillation within cross sections as they move along the jet axis. If the liquid is inviscid and the oscillations have infinitesimal amplitude,

$$\omega_n = 2\pi f_n = \sqrt{\frac{(n^3 - n)\gamma}{\rho a^3}}, \quad (5)$$

where  $\rho$  is the density of the liquid,  $\gamma$  is the coefficient of surface tension, and  $f_n$  is the frequency of a pure mode  $n$ . Formula (5) will of course require correction for additional effects such as viscosity, the inertia of the surrounding air, gravity, small wavelengths, and large amplitudes  $b_n/a = O(1)$ .

The dominant wavenumber of the chain oscillations can be inferred from the elliptical shape of the nozzle. The Fourier expansion of an ellipse  $R(\phi, z)$  is dominated by the  $n = 2$  term, with additional smaller terms  $n = 4, 6, \dots$ . The  $n = 2$  term corresponds to stretching along one axis and shortening along the perpendicular axis. We therefore expect chain oscillations to be dominated by the  $n = 2$  term.

The remaining modes  $n \geq 3$  produce polygonlike shapes with  $n$  maxima and  $n$  minima distributed around the circle (see Fig. 3). The amplitude (elongation) for which a given shape most closely resembles a polygon is that for which the curvature at the local minimum vanishes, which

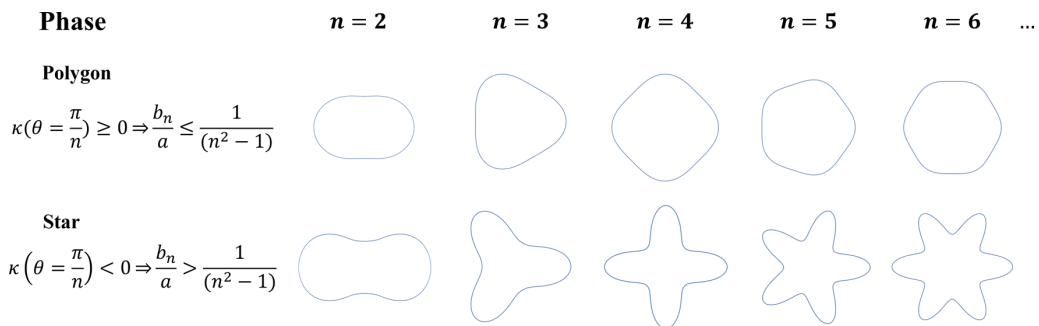


FIG. 3. Shapes  $R_n(\theta) = a + b \cos n\theta$  of the normal modes of oscillation of a capillary jet.  $\theta = 0$  is along the positive  $x$  axis.

occurs when  $\varepsilon := b/a = 1/(n^2 - 1)$ . At larger elongations, the curvature at the local minima is negative, resulting in starlike shapes. For  $n = 2$  the shape resembles a peanut. For each pure mode the cross section will appear to rotate by an angle  $\pi/n$  after each half oscillation, or

$$R_n(\theta, z) = R_n\left(\theta \pm \frac{\pi}{n}, z \pm \frac{\lambda}{2}\right). \quad (6)$$

For  $n = 2$ , the long axis of the cross section appears to rotate by  $\pi/2$  after each half oscillation, inspiring the description “axis switching” for this case.

Because the  $n = 1$  mode represents the displacement of the cross section’s center of mass, the  $n = 2$  mode is the fundamental mode of vibration of a liquid jet. This is why it is observed so often in nature: it is the easiest vibrational mode to excite. Even if the perturbation contains significant energy for  $n \geq 3$ , as long as the  $n = 2$  is dominant the jet will behave very similarly to a “pure” chain oscillation. This explains, for example, why these oscillations are excited in pouring a liquid, as illustrated in Fig. 1. The linear theory suggests that the initial amplitude of mode  $n = 2$  can be determined from the aspect ratio  $(a + b_2)/(a - b_2)$  of the orifice.

#### IV. EXPERIMENT: MATERIALS AND METHODS

A vertical liquid chain can easily be produced by forcing a steady laminar flow through a horizontal elliptical orifice. Here we study chain oscillations in water using 12 different orifices with major axes 1–4 cm and eccentricities 0.75–0.99. Their specifications can be found in Table I. Our first task is to generate jets that are sufficiently smooth to undergo several turns or axis switches before breaking up. It is not sufficient to have a very smooth nozzle as described by Bergthorson *et al.* [24], since we need to produce a long laminar jet after the orifice: The flow needs to be prelaminarized before exiting the orifice. We do this by passing the water through a plexiglass cylinder 6 cm in diameter and 10 cm in length, filled with drinking straws and with porous sponges at both the inlet and the outlet. The latter is an elliptical hole machined precisely in a thin stainless steel sheet. Jets formed in this way are very smooth, and break up roughly 1 m from the orifice for our experimental conditions. A schematic view of the experimental setup is shown in Fig. 4.

Because we use a fixed liquid (water) and a rigid orifice, maintaining stable jetting conditions requires a fixed flow rate  $Q$ , our control parameter. The liquid is supplied from a tank pressurized with nitrogen to a constant but adjustable level, typically around 5 bars. This liquid is then routed through a hand-operated valve that controls the flow rate, and an electromagnetic flowmeter (Krohne) measures the flow rate. After setting  $Q$  to the desired value, we found that the fluid chain became stationary after a brief ( $\approx 1$  s) transient period needed for the pressure distribution in the setup to equilibrate. Typical values of the Reynolds number  $\text{Re} = Q/R_{\text{eq}} \nu$  in our experiments are  $10^3 \lesssim \text{Re} \lesssim 20 \times 10^3$ , where  $R_{\text{eq}} \equiv \sqrt{D_x D_y}/2$  and  $\nu$  is the kinematic viscosity of water. Note that

TABLE I. Geometrical properties of the orifices used to generate chain oscillations.

Orifice No.	Major axis, $D_x$ (cm)	Minor axis, $D_y$ (cm)	Eccentricity	Orifice area, $A$ (cm <sup>2</sup> )	$\Pi_3/10^5$	$\Pi_4$
1	1	0.44	0.9	0.34	2.31	71
2	1	0.31	0.95	0.25	1.95	60
3	2	0.62	0.95	0.98	3.91	120
4	2	0.28	0.99	0.44	2.63	80
5	4	1.74	0.9	5.48	9.24	283
6	4	1.25	0.95	3.92	7.82	239
7	4	0.56	0.99	1.77	5.26	161
8	1.5	1	0.75	1.18	4.29	131
9	2	1.5	0.66	3.14	6.06	185
10	3	1	0.94	2.36	6.06	185
11	3	1.5	0.87	3.53	7.42	227
12	3	1.9	0.77	4.48	8.36	255

Re is equal to  $\pi$  times the usual Reynolds number  $W_0 R_{\text{eq}}/\nu$  where  $W_0$  is the exit velocity at the orifice.

Figure 5(b) shows the morphology of the chain for orifice number 11 and ten values of  $Q$ . The wavelength of the chain oscillations increases with increasing flow rate. Note also that the surface of the liquid chain becomes increasingly irregular as  $Q$  increases.

Here we focus on measuring the frequency of chain oscillations as a function of flow rate and comparing it to theoretical predictions. At steady state, conservation of volume flux implies that

$$Q = W(z)A(z), \quad (7)$$

where  $A(z)$  is the cross-section area of the jet. The time  $\Delta t$  required to travel a distance equal to one wavelength starting from a point  $z = z_0$  is

$$\Delta t = \int_{z_0}^{z_0+\lambda} \frac{dz}{W(z)} \equiv \frac{1}{f_\lambda}, \quad (8)$$

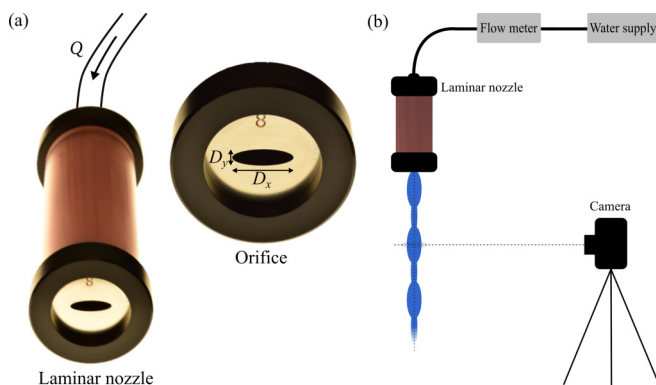


FIG. 4. Laboratory setup for chain oscillations. (a) Laminar flow nozzle used to generate a smooth jet. The flow rate  $Q$  is controlled using a pressurized tank and a flowmeter. The right image illustrates the major and minor axes  $D_x$  and  $D_y$  of the elliptical orifice. (b) Schematic of the experimental setup.



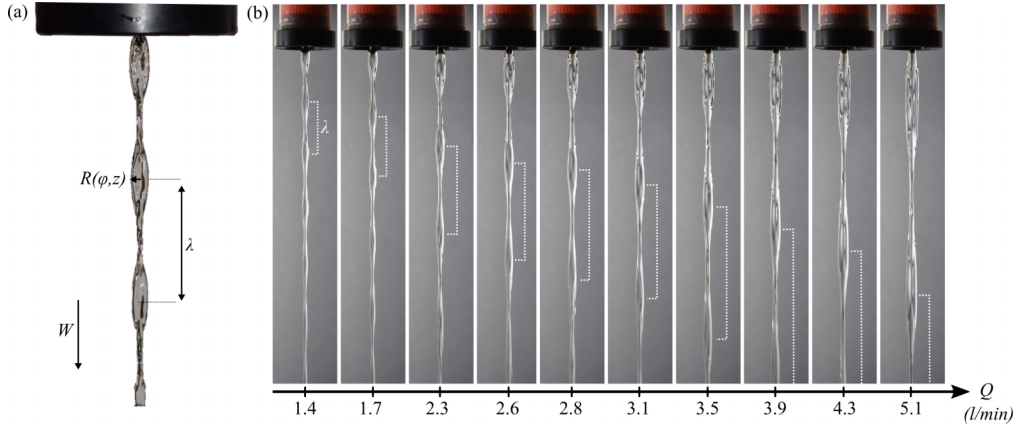


FIG. 5. Dependence of steady chain oscillations on the flow rate. (a) Schematic diagram indicating the jet velocity  $v_z$ , the local radius  $R(\phi, z)$ , and the wavelength  $\lambda$ . (b) Observed morphology of the chain oscillations as a function of flow rate  $Q$  for an elliptical orifice with major axis 3 cm and minor axis 1.5 cm. The wavelength  $\lambda$  of the chain is indicated on each image.

where we denote by  $f_\lambda$  the chain oscillation frequency calculated from the measured wavelength. Using Eq. (7) to eliminate  $W(z)$  from Eq. (8), we obtain

$$f_\lambda = Q \left[ \int_{z_0}^{z_0+\lambda} A(z) dz \right]^{-1} \equiv \frac{Q}{V_\lambda}, \quad (9)$$

where  $V_\lambda$  is the volume of fluid contained in one wavelength of the jet.

The next step is to determine whether  $f_\lambda$  agrees with theoretical predictions. Assuming that chain oscillations correspond to the mode  $n = 2$ , we see from Eqs. (4) and (5) that Rayleigh's linear theory predicts

$$R(\theta, t)_{\text{Rayleigh}} = a - \frac{b^2}{8a} + b \cos 2\theta \cos \omega t, \quad (10a)$$

$$f_{\text{Rayleigh}} = \frac{1}{2\pi} \sqrt{\frac{6\gamma}{\rho a^3}}. \quad (10b)$$

More sophisticated theoretical predictions can be obtained by correcting Eqs. (10) to account for the additional effects mentioned previously. However, we found that in our case the only significant correction is due to large dimensionless amplitudes  $\epsilon = b/a$  (see Discussion). An elegant analytical solution valid to  $O(\epsilon^2)$  was obtained by Bohr [5], and is

$$R(\theta, t)_{\text{Bohr}} = R(\theta, z)_{\text{Rayleigh}} + \frac{b^2}{a} \left( \frac{1}{6} \cos 4\theta \cos 2\omega t + \frac{1}{4} \cos 4\theta - \frac{1}{8} \cos 2\omega t \right), \quad (11a)$$

$$f_{\text{Bohr}} = f_{\text{Rayleigh}} \sqrt{1 - \frac{37}{24} \frac{b^2}{a^2}}. \quad (11b)$$

Bohr's solution predicts that the frequency depends on the amplitude  $b$  of the oscillation, which is a generic feature of nonlinear oscillations.

Figure 6 shows the shape of the cross section of the jet predicted by Bohr's theory for  $n = 2$  and several values of the dimensionless amplitude  $b/a$ . The case  $b/a = 0$  corresponds to the linear theory of Rayleigh. For  $b/a > 0.3595$ , the shape profile becomes reentrant and  $x(y)$  is multivalued (see the Appendix for the derivation).



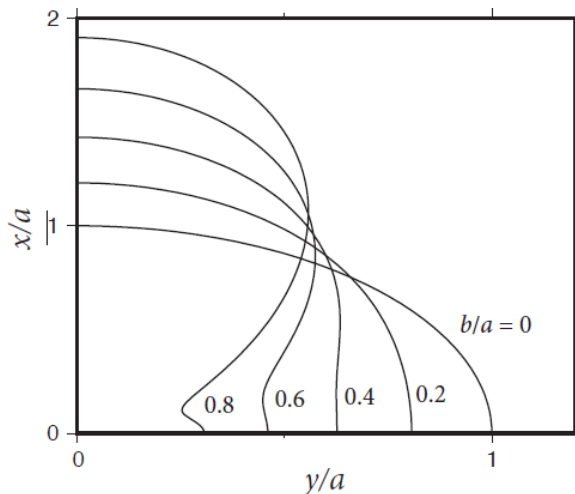


FIG. 6. Shape of the jet cross section for  $\omega t = 2m\pi$  ( $m$  is an integer) and a single mode  $n = 2$  predicted by the nonlinear theory of Bohr [5], for several values of the dimensionless amplitude  $b/a$ . The curves are given by Eq. (A38). The horizontal scale is exaggerated by a factor of 2 relative to the vertical scale. The curve  $x(y)$  is multivalued when  $b/a > 0.3595$ .

Equation (9) showed that the frequency  $f_\lambda$  is inversely proportional to the volume  $V_\lambda$  of fluid contained within one wavelength of the chain. In order to estimate  $V_\lambda$  for each of our experiments, we make use of the theoretical expressions (10a) and (11a). Substituting either of these expressions into the definition (9) of  $V_\lambda$  gives  $V_\lambda = \pi a^2 \lambda$  to within a small relative error of at most order  $(b/a)^2$ . Equation (9) then becomes

$$f_\lambda = \frac{Q}{\pi a^2 \lambda}. \quad (12)$$

To estimate  $a$  for our experiments, we measure the minimum and maximum radii  $R_{\min}$  and  $R_{\max}$  over one wavelength of the chain, using photographs taken parallel to the major axis of the orifice. The amplitudes  $a$  and  $b$  are then determined by solving two simultaneous linear equations with slightly different forms depending on whether we use Rayleigh's or Bohr's expression for  $R(\phi, t)$ . The equations for these two cases are

$$\begin{aligned} \text{Rayleigh: } & \begin{cases} \frac{1}{2}(R_{\max} - R_{\min}) & = b \\ \frac{1}{2}(R_{\max} + R_{\min}) & = a \left(1 - \frac{1}{8} \frac{b^2}{a^2}\right), \end{cases} \\ \text{Bohr: } & \begin{cases} \frac{1}{2}(R_{\max} - R_{\min}) & = b \\ \frac{1}{2}(R_{\max} + R_{\min}) & = a \left(1 + \frac{1}{6} \frac{b^2}{a^2}\right). \end{cases} \end{aligned} \quad (13)$$

We find that the inferred values of  $a$ ,  $b$ , and  $b/a$  all increase with increasing flow rate.

## V. EXPERIMENT VERSUS THEORY

Figure 7(a) compares our inferred frequencies  $f_\lambda$  (circles) with the frequencies  $f_{\text{Rayleigh}}$  (black line) and  $f_{\text{Bohr}}$  (light grey line). The decrease of all three frequencies with increasing flow rate is evident. This is due to the increase of  $a$  and  $b/a \in [0.08, 1.67]$  with  $Q$  (see tables in the Supplemental Material [25]), which reduces the frequency according to Eqs. (9), (10b), and (11b). Second, we see that Bohr's corrected formula (11b) agrees much better with the observations than does Rayleigh's infinitesimal-amplitude formula (10b). Bohr's formula matches the observations within the experimental uncertainties, even though it is only valid up to second order in amplitude.

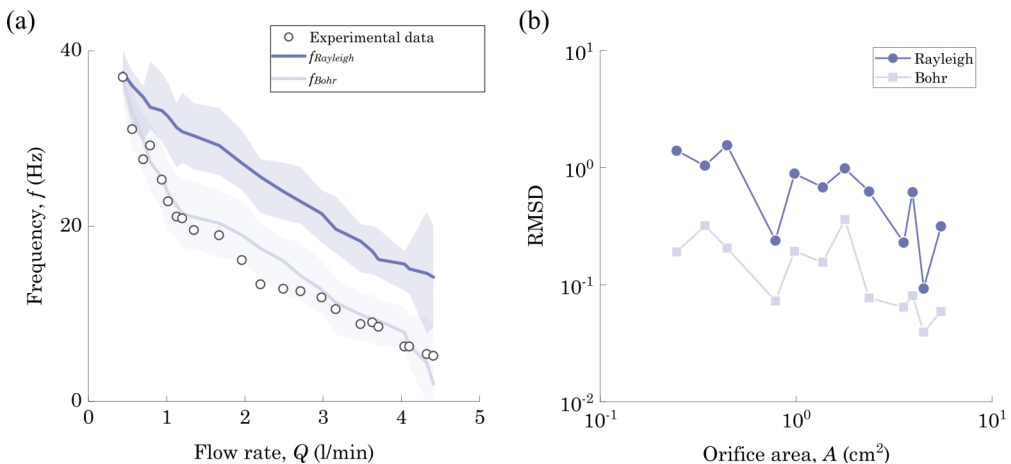


FIG. 7. Comparison of the theoretical estimates of Rayleigh and Bohr. (a) Frequency  $f$  of chain oscillations as a function of the flow rate and for orifice 7 with  $D_x = 4$  cm and  $D_y = 1.74$  cm. Continuous lines are the prediction from Rayleigh [Eq. (10b)] and Bohr [Eq. (11b)]. (b) Root mean square deviation (RMSD) comparing the accuracy of Eqs. (10b) and (11b) for all 12 orifices. The RMSD is plotted as a function of the (unique) orifice area.

The close agreement between our observations and Bohr’s finite-amplitude theory holds good for all the orifices we used. Figure 7(b) shows a measure of the error of the theoretical frequency (either Rayleigh’s or Bohr’s) for the different orifices, each distinguished by its unique area. The error is expressed as a normalized root mean square deviation (RMSD) defined as

$$\text{RMSD} := \sqrt{\frac{1}{N} \sum_{i=1}^N \left( \frac{f_{\lambda}^{(i)}}{f_{\text{Bohr/Rayleigh}}^{(i)}} - 1 \right)^2}, \quad (14)$$

where the sum is over all flow rates  $Q_i$  used for a given orifice. That sum is then normalized by the number  $N$  of flow rates and the square of the measured value of the frequency, so that the summed discrepancies between theory and experiment are dimensionless and comparable for different orifices. The RMSD values of Fig. 7(b) show that Bohr’s formula fits observations much better than Rayleigh’s, and about equally so for different orifices. In summary, Fig. 7 implies that fluid chains are indeed nonlinear oscillations for which the frequency of oscillation depends on the amplitude. Due to the nonlinearity of the boundary condition representing surface tension, chain oscillations are only isochronous for very small amplitudes.

## VI. DIRECT NUMERICAL SIMULATION

We performed direct numerical simulations of chain oscillations using the volume-of-fluid code Gerris Flow Solver (GFS [26]). To illustrate, we use the parameters of the experiments with flow rates  $Q = 1.41$  and  $2.82$  l min<sup>-1</sup> with orifice number 11. Figure 8(a) shows the shape of the experimental jet with  $Q = 1.41$  l min<sup>-1</sup>, and Fig. 8(b) shows the shape and thickness of the corresponding numerically simulated jet. The shapes of the experimental and simulated jets agree very well, although the amplitude of the chain links is somewhat greater in the simulation than in the experiment. For comparison, Fig. 8(c) shows the shape and thickness of the jet predicted by Bohr’s theory, with an amplitude  $b = 0.66a$  chosen to match the observed wavelength of the chain oscillations. The resulting shape agrees well with that of the numerical simulation in Fig. 8(b). However, it is worth noting that the dimensionless amplitude  $b/a = 0.66$  is much larger than the corresponding Fourier coefficient of the nozzle shape. For the experiment in question, the shape of

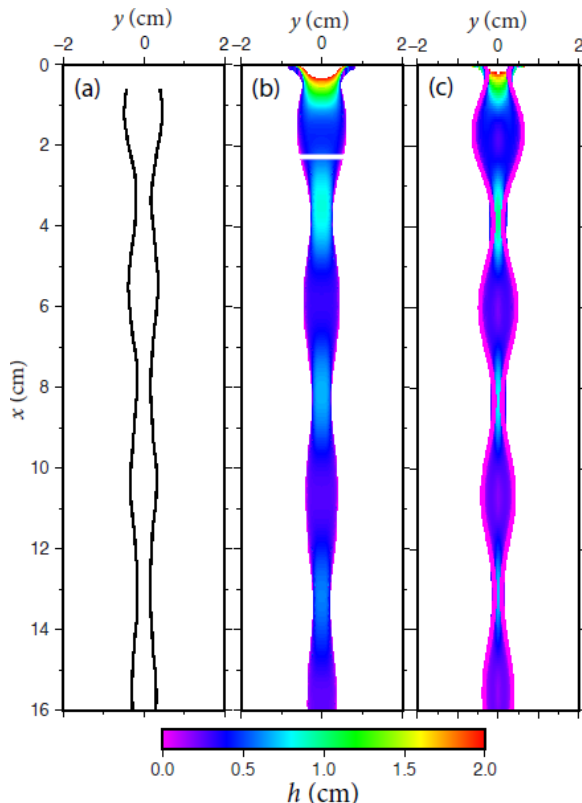


FIG. 8. Shape and thickness of a jet with flow rate  $Q = 1.41 \text{ l min}^{-1}$  falling from an elliptical nozzle with semiminor axis 0.75 cm and semimajor axis 1.5 cm. The major axis is perpendicular to the plane of the page. (a) Shape of the jet observed in the experiment. (b) Shape and thickness  $h$  of the numerically simulated jet. The white portion near the top corresponds to thicknesses  $2.0 < h < 3.0$  cm. The white horizontal bar indicates the location of the cross section that is examined in more detail in Fig. 9. (c) Shape and thickness of the jet predicted by Bohr's theory with  $b/a = 0.66$ . The time  $t$  in Bohr's theory is related to the downstream distance  $z$  by the free-fall expression  $t = (-W_0 + \sqrt{W_0^2 + 2gz})/g$ , where  $W_0$  is the vertical velocity at the orifice.

the nozzle has the Fourier expansion

$$R_{\text{nozzle}} = R_{\text{eq}} (0.9708 + 0.3284 \cos 2\theta + 0.0825 \cos 4\theta + \dots), \quad (15)$$

where  $R_{\text{eq}} = 1.061$  cm is the nozzle's equivalent radius. Comparing Eq. (15) with Eq. (4) with  $n = 2$ , we see that Eq. (15) implies  $(b/a)_{\text{nozzle}} = 0.333$ , which is half the value  $b/a = 0.66$  that best fits the observed axis switching wavelength.

Figure 9 shows the in-plane velocity components  $u(x, y)$  and  $v(x, y)$  in the section of the simulated jet indicated by the white line in Fig. 8(b). The velocity is outward along the  $x$  axis and inward along the  $y$  axis. This indicates that the section is undergoing elongation in the  $x$  direction and shortening in the  $y$  direction, which is compatible with an in-plane oscillation.

Figure 10 is the same as Fig. 8 except that the flow rate is now  $Q = 2.82 \text{ l min}^{-1}$ . The chain wavelength predicted by the numerical simulation [Fig. 10(b)] agrees reasonably well with the observed wavelength. However, a significant phase shift is evident: the simulated chain links are displaced downward relative to the observed ones. On the other hand, the prediction of Bohr's theory with  $b/a = 0.70$  [Fig. 10(c)] looks remarkably similar to the numerical simulation, the only significant difference being an underestimation of the minimum width relative to the simulation.

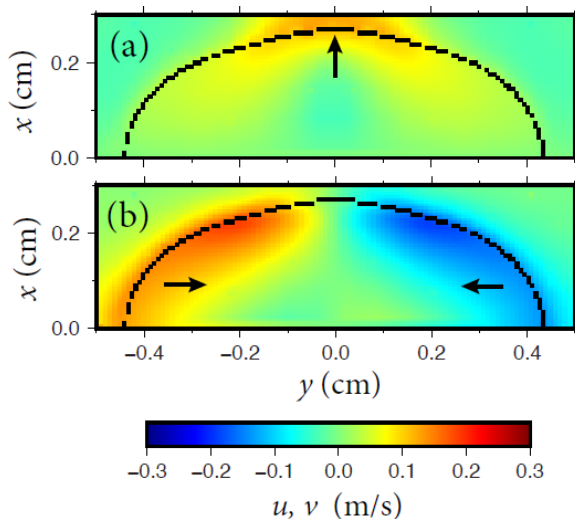


FIG. 9. In-plane velocity components (a)  $u(x, y)$  and (b)  $v(x, y)$  in the horizontal cross section shown by the horizontal white bar in Fig. 8(b). The black lines indicate the water/air interface. The jaggedness of those lines reflects the finite numerical resolution of the interface. Arrows show the directions of the velocity.

## VII. CROSS-SECTION SHAPE OF THE CHAIN VERSUS ORIFICE SHAPE

In the previous section, we saw that the amplitude  $b/a$  in Bohr's theory that best fits finite-volume simulations can be very different from the value of  $b/a$  that corresponds to the quadrupole ( $n = 2$ ) Fourier coefficient of the orifice shape. Accordingly, in this section we quantify in more detail the relation between the experimentally determined value of  $b/a$  and the shape of the orifice. We proceed by dimensional analysis. The normalized amplitude  $b/a$  of the chain oscillations observed in our experiments can depend on  $Q$ ,  $g$ ,  $\nu$ ,  $\gamma$ ,  $\rho$ ,  $D_x$ , and  $D_y$ . We seek to determine the unknown function  $f_1$  defined by

$$\frac{b}{a} = f_1(Q, g, \nu, \gamma/\rho, D_x, D_y). \quad (16)$$

Because  $\gamma$  and  $\rho$  are the only parameters involving units of mass, they can appear only as the quotient  $\gamma/\rho$ . Now of the six arguments of  $f_1$ , two have independent dimensions. According to Buckingham's  $\Pi$  theorem, four independent dimensionless groups can be formed from the six arguments. We choose these to be

$$\Pi_1 = \frac{Q}{R_{\text{eq}}\nu}, \quad \Pi_2 = \left[1 - \left(\frac{D_y}{D_x}\right)^2\right]^{1/2}, \quad \Pi_3 = \frac{\gamma R_{\text{eq}}}{\rho\nu^2}, \quad \Pi_4 = R_{\text{eq}}\left(\frac{g}{\nu^2}\right)^{1/3}, \quad (17)$$

where  $R_{\text{eq}} = \sqrt{D_x D_y}/2$ . Note that we have chosen the definitions of the groups such that  $\Pi_2$ ,  $\Pi_3$ , and  $\Pi_4$  are all constant for a series of experiments with a given orifice and a variable flow rate.  $\Pi_1$  is proportional to the Reynolds number.  $\Pi_2$  is the eccentricity of the orifice, and is given in column 4 of Table I. The values of  $\Pi_3$  and  $\Pi_4$  for each of our series of experiments are given in columns 6 and 7 of Table I. Equation (16) is now equivalent to

$$\frac{b}{a} = f_2(\Pi_1, \Pi_2, \Pi_3, \Pi_4), \quad (18)$$

where  $f_2$  is an unknown function.

Figure 11 shows  $b/a$  vs  $\Pi_1$  for five sets of experiments with different nozzles. Two pairs of these experiments have the same or nearly the same values of the orifice eccentricity  $\Pi_2$ . For each of

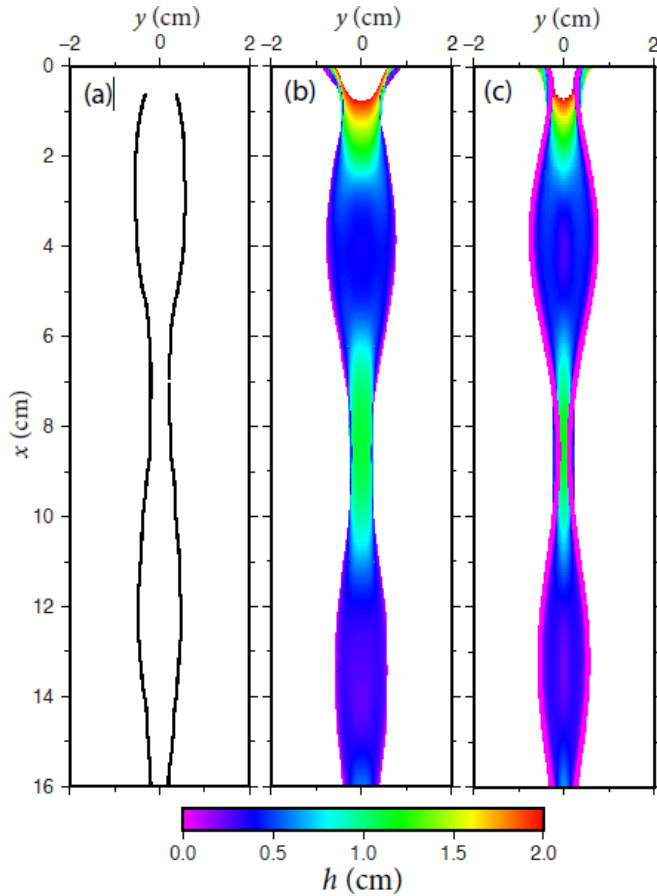


FIG. 10. Same as Fig. 8, but for a flow rate  $Q = 2.82 \text{ l min}^{-1}$ . (c)  $b/a = 0.70$ .

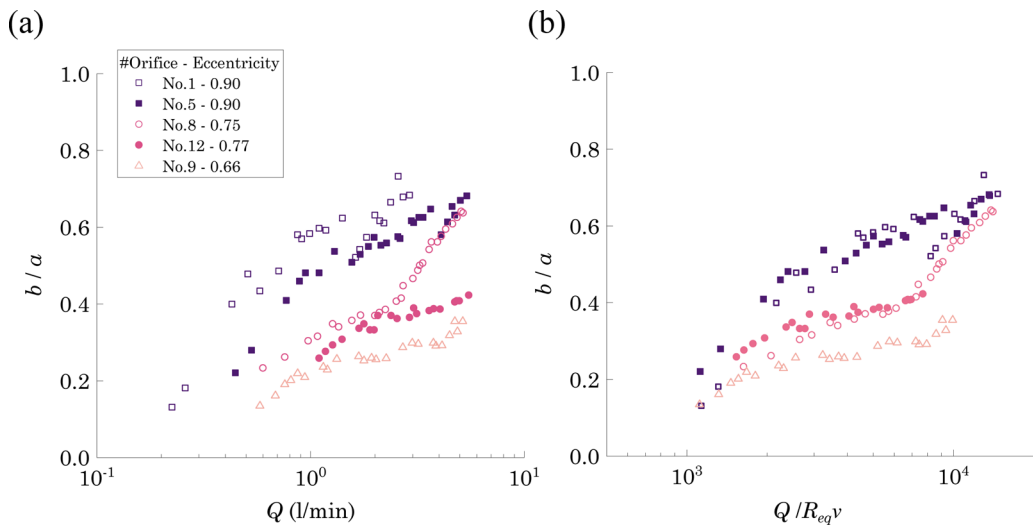


FIG. 11. (a) Normalized amplitude  $b/a$  observed experimentally as a function of the flow rate  $Q$  for five different orifices with different eccentricities. (b) Normalized amplitude as a function of  $\text{Re} \equiv Q/\nu R_{eq}$ .

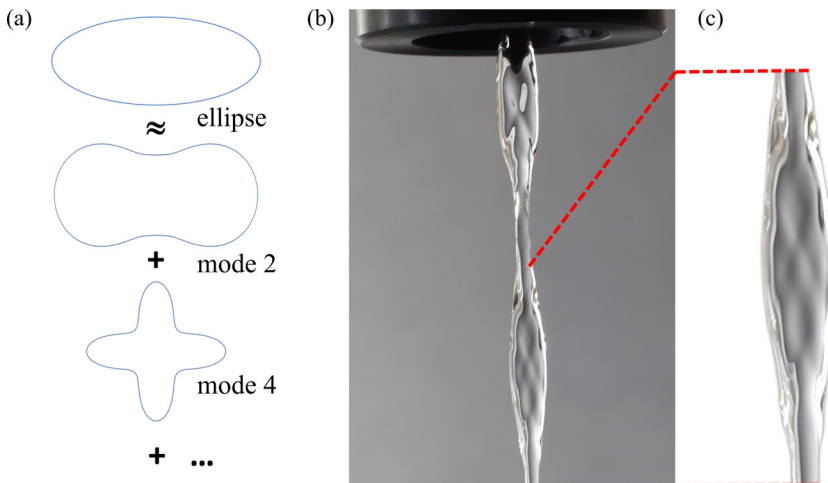


FIG. 12. Presence of higher-order modes. (a) Illustration of the ellipse as a sum of different normal modes. Modes  $n = 2$  and  $n = 4$  are displayed at large amplitudes, to demonstrate that an elliptical orifice excites higher-order modes of oscillation. (b) Photograph of chain oscillations at large amplitude displaying a component of mode  $n = 4$ . This is observed for jet with flow rate  $Q = 1.30 \text{ l min}^{-1}$  falling from an elliptical nozzle with semiaxes 0.31 and 1 cm. (c) Zoom of (b). The four bumps over a link correspond to a component of mode  $n = 4$  superimposed on a chain oscillation with  $n = 2$ .

the three eccentricities the collapse of the data is reasonably good given the scatter, suggesting that Eq. (18) can be reduced to

$$\frac{b}{a} = f_3(\Pi_1, \Pi_2). \quad (19)$$

Equation (19) implies that  $b/a$  depends on both the flow rate and the eccentricity of the orifice.

### VIII. HIGHER-ORDER MODES

As Eq. (15) shows, the Fourier expansion of the shape of an elliptical nozzle contains not only the dominant harmonic  $\cos 2\theta$ , but also the higher even harmonics  $\cos 4\theta$ ,  $\cos 6\theta$ , etc. The presence of these harmonics should excite chain oscillations with azimuthal wavenumbers  $n = 4, 6$ , etc. in addition to the dominant oscillation with  $n = 2$ . In fact, the presence of the mode  $n = 4$  in our experiments can be observed with the naked eye. Figure 12 shows a close-up photograph of a chain link in a jet with a flow rate  $Q = 1.30 \text{ l min}^{-1}$  exiting a nozzle with semimajor axis 1 cm and semiminor axis 0.31 cm. Three symmetrically disposed bumps are visible on the surface of the chain over a link length.

To understand the origin of the bumps, we extend the nonlinear analysis of Bohr [5] to the case of two interacting modes  $n = 2$  and  $n = 4$ . This is done in the Appendix using a regular perturbation expansion together with solvability conditions. Denoting the amplitudes of the two base modes by  $b_2$  and  $b_4$  and their frequencies by  $\omega_2$  and  $\omega_4$ , we find that the jet's shape is

$$\begin{aligned} R(\theta, t) = & a + b_2 \cos 2\theta \cos \omega_2 t + b_4 \cos 4\theta \cos \omega_4 t + \frac{b_2^2}{24a} [6 \cos 4\theta - 3 + (4 \cos 4\theta - 3) \cos 2\omega_2 t] \\ & + \frac{b_4^2}{616a} [11(22 \cos 8\theta - 7) - 7(4 \cos 8\theta + 11) \cos 2\omega_4 t] \\ & + \frac{b_2 b_4}{1608a} \cos 2\theta [\sqrt{10}(378 \cos 4\theta - 55) \sin \omega_2 t \sin \omega_4 t \\ & + 2(1752 \cos 4\theta - 1747) \cos \omega_2 t \cos \omega_4 t], \end{aligned} \quad (20)$$

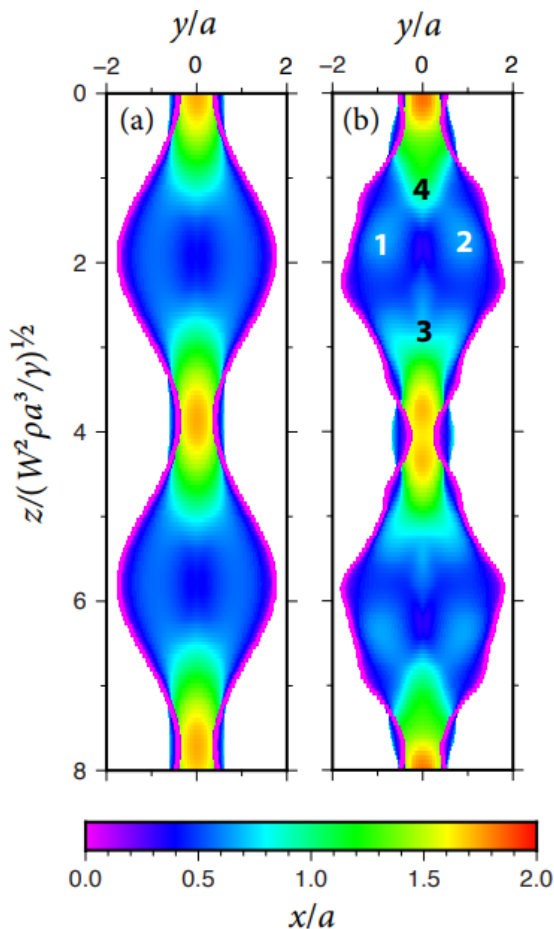


FIG. 13. Coordinates  $x(y, z)$  of the surface of the jet defined by Eqs. (20)–(22), for  $b_2/a = 0.66$  and  $b_4/a =$  (a) 0.0 and (b) 0.1. Labels 1–4 indicate maxima of  $x(y, z)$ .

where

$$\omega_2 = \sqrt{\frac{6\gamma}{\rho a^3}} \left( 1 - \frac{37}{48} \frac{b_2^2}{a^2} - \frac{19325}{6432} \frac{b_4^2}{a^2} \right), \quad (21)$$

$$\omega_4 = 2 \sqrt{\frac{15\gamma}{\rho a^3}} \left( 1 - \frac{4575}{1232} \frac{b_4^2}{a^2} - \frac{3865}{6432} \frac{b_2^2}{a^2} \right). \quad (22)$$

The term  $\propto b_2 b_4$  in Eq. (20) accounts for the nonlinear interaction of the two modes. Another sign of the interaction is that each frequency  $\omega_2$  and  $\omega_4$  depends on both amplitudes  $b_2$  and  $b_4$ .

To recast Eqs. (20)–(22) in dimensionless form, we first transform time to distance  $z = Wt$ , where the jet speed  $W$  is assumed constant for simplicity. Next, we define dimensionless frequencies  $\hat{\omega}_n = \sqrt{\rho a^3 / \gamma} \omega_n$  and a dimensionless distance  $\hat{z} = W^{-1} \sqrt{\gamma / \rho a^3} z$ . The dimensionless jet radius  $R/a \equiv \hat{R}$  then depends only on  $\hat{z}$ ,  $\theta$ , and the two dimensionless amplitudes  $b_2/a$  and  $b_4/a$ .

Figure 13 shows the dimensionless normal coordinate  $\hat{x} = \hat{R} \sin \theta$  of the jet's surface as a function of  $\hat{z}$  and the dimensionless lateral coordinate  $\hat{y} = \hat{R} \cos \theta$  for  $b_2/a = 0.66$  and  $b_4/a = 0$  [Fig. 13(a)] and  $b_4/a = 0.1$  [Fig. 13(b)]. For  $b_4 = 0$ , each link exhibits maxima in the form of continuous bands (light blue). For  $b_4 = 0.1a$ , however, the bands are replaced by two isolated maxima (light blue,



labeled 1 and 2). These maxima are generated by the term  $b_4 \cos 4\theta \cos \omega_4 t$  in Eq. (20). The other two maxima (labeled 3 and 4) centered on  $y = 0$  are, however, not isolated but blend continuously into the neighboring links. In summary, our generalization of Bohr’s solution predicts qualitatively the distribution of bumps on the jet surface associated with the mode  $n = 4$ , without, however, reproducing the nearly perfect symmetry of the experimental observations (Fig. 12).

## IX. DISCUSSION

Our chain-oscillation experiments were performed under laminar flow conditions, enforced by a “straws and sponges” device at the flow inlet. Moreover, in most of our experiments, the typical wavelength of axis switching was large compared to the effective radius  $R_{\text{eq}}$  of the jet. Finally, because the aspect ratio of our elliptical nozzles was typically two or more, the amplitude of the observed chain oscillations was not small relative to  $R_{\text{eq}}$ . The three conditions just mentioned are precisely those envisioned by Bohr’s nonlinear theory of chain oscillations [5], which led us to compare our observations to Bohr’s theoretical predictions in some detail. We found that the measured frequency of axis switching agreed with Bohr’s prediction within experimental uncertainty for all the nozzles we used. By contrast, we found that Rayleigh’s linear theory [2] disagreed with our observations, even allowing for the experimental uncertainty. We conclude that the axis switching in our experiments is due to the nonlinear oscillation of 2D cross sections of the jet, with a frequency that depends on the amplitude of the oscillation. The agreement between experiment and theory further shows that the chain oscillations we observed are dominated by the azimuthal mode  $n = 2$ .

Our results are consistent with those of Moon *et al.* [17], who found that direct observations of the shape of oscillating jets agreed closely with Bohr’s theoretical predictions. Moon *et al.* used two independent methods—optical forward diffraction and cavity resonance spectroscopy—to estimate the ratio of the octapolar component ( $\propto \cos 4\theta$ ) to the quadrupolar component ( $\propto \cos 2\theta$ ) of the surface shape. By evaluating Eq. (11a) at  $t = 0$ , one sees that Bohr’s theory predicts this ratio to be  $Bb/a$  where  $B = 5/12 \approx 0.417$ . Moon *et al.*’s two sets of measurements yielded  $B = 0.42 \pm 0.08$  and  $B = 0.414 \pm 0.011$ .

Despite the excellent agreement between experiment and Bohr’s nonlinear theory found by Moon *et al.* [17] and ourselves, the theory has limitations that need to be kept in mind. The first is that it does not take into account the viscosity of the jet. However, Bohr [5] used a linearized model to estimate the length scale  $z_{\text{visc}}$  of exponential decay along the jet axis of oscillations with azimuthal wavenumber  $n$ . For  $n = 2$ , Eq. (40) on page 289 of [5] gives

$$z_{\text{visc}} = \frac{R_{\text{eq}}^2 W}{4\nu} = \frac{Q}{4\pi\nu}, \quad (23)$$

where  $\nu$  is the kinematic viscosity of the jet fluid. For our experiments  $\nu = 1 \text{ cS}$  and  $Q = 1\text{--}4 \text{ l min}^{-1}$ , wherefore  $z_{\text{visc}} \approx 1\text{--}5 \text{ m}$ . These lengths are many times greater than the observed wavelengths of the chain oscillations, which implies that the effect of viscosity is negligible. However, theoretical models including viscosity have been developed for fluid chain formation following collision of laminar viscous jets [21], and it would be interesting to compare that theory with an extended version of Bohr’s theory that includes viscosity.

Another limitation of Bohr’s nonlinear theory is that it does not account for the inertia of the air surrounding the jet. However, Bohr [5] uses a linearized model to show that this effect is of magnitude  $\rho_{\text{air}}/\rho_{\text{jet}}$  relative to the inertia of the jet itself. For a jet of water,  $\rho_{\text{air}}/\rho_{\text{jet}} = 0.00123$ , implying that the inertia of the air is negligible.

A further limitation of Bohr’s theory is that it includes only the first correction to Rayleigh’s linear theory, i.e., terms of second order in the dimensionless amplitude  $b_n/a$ . Bohr’s theory is therefore valid only if  $(b_n/a)^2$  is small. However, Figs. 8 and 10 show that values  $(b_2/a)^2 \approx 0.44\text{--}0.49$  are necessary for Bohr’s theory to match the results of direct numerical simulations. These values of  $(b_2/a)^2$  are rather large, and imply that Bohr’s theory may be only roughly applicable. We anticipate that the situation would be even worse for nozzles having aspect ratios (ARs) larger than

the one used for Figs. 8 and 10, which was  $AR = 2$ . The situation could be improved by extending Bohr’s approach to order  $(b_2/a)^4$ , following the method of our Appendix. However, this lengthy calculation is beyond our scope here.

A final limitation of Bohr’s theory is that it assumes purely 2D flow in the plane of the cross section of the jet or (equivalently) that the wavelength of axis switching is large compared to the jet’s typical equivalent radius  $R_{\text{eq}}$ . This assumption is likely to be invalid in the near-nozzle region, where cross sections evolve rapidly with downstream distance. One manifestation of this is that the water in our experiments exits the nozzle not at  $90^\circ$ , but rather at a smaller angle  $\theta_{\text{exit}}$  that depends on the flow rate. This, together with the gravity-induced stretching of the jet, means that  $R_{\text{eq}}(z)$  rapidly decreases with downstream distance over a lengthscale that is not large compared to a typical value of  $R_{\text{eq}}$ . This may explain the observation of Bohr [5] that the wavelength of the first chain link is always a bit shorter than what he calculated it should be. This fact was attributed by Bohr [5] to the “formation of the jet” and by Kasyap *et al.* [9] to the “presence of the orifice.”

To conclude, we note that all the nozzle shapes commonly used in studies of chain oscillations—elliptical, square, rectangular, and triangular—have Fourier expansions containing a dominant mode ( $n = 2, 3$ , or  $4$ ) plus higher harmonics. The presence of the higher harmonics means that the nozzle generates “impure” oscillations in which two or more azimuthal modes interact. In future, it would be desirable to study “pure” chain oscillations by performing experiments with nozzles specially designed to contain only a single Fourier mode  $n \geq 2$  in addition to the constant term  $n = 0$ .

### ACKNOWLEDGMENTS

We are much indebted to J. Eggers for very helpful discussions. We thank the machine shop of the Institute of Physics of the University of Amsterdam for technical assistance. N.M.R. thanks the University of Amsterdam for a two-month visiting professorship during which much of this work was done.

### APPENDIX: TWO-MODE ANALYTICAL SOLUTION

Bohr [5] examined the problem of the finite-amplitude oscillation of a two-dimensional inviscid fluid disk with surface tension acting on its circumference. Using a method of successive approximations due to Stokes, Bohr determined the time-dependent shape of the disk to  $O((b/a)^2)$ , where  $b$  is the amplitude of the solution to the linearized problem. He also found an expression for the frequency  $\omega_n(b)$  of the oscillation to the same order of approximation. In the following sections we generalize Bohr’s problem to the case of two interacting modes, using a more modern approach involving a systematic perturbation expansion together with solvability conditions.

#### 1. Governing equations

First we introduce Cartesian coordinates  $(x, y, z)$  such that  $z$  is the vertical coordinate and  $x$  and  $y$  are along the major and minor axes of the elliptical nozzle, respectively. We also introduce polar coordinates  $(r, \theta)$  in the  $x$ - $y$  plane such that  $\theta = 0$  is along the  $x$  axis.

Let  $u$  be the radial velocity and  $v$  be the azimuthal velocity in a horizontal cross section of the jet. Define a velocity potential  $\phi$  such that

$$u = -\partial_r \phi, \quad v = -\frac{1}{r} \partial_\theta \phi. \quad (\text{A1})$$

The continuity equation reduces to

$$\nabla^2 \phi = 0 \quad (\text{A2})$$

and the pressure is

$$p = \rho \left\{ \partial_t \phi - \frac{1}{2} \left[ (\partial_r \phi)^2 + \frac{1}{r^2} (\partial_\theta \phi)^2 \right] \right\} + F(t). \quad (\text{A3})$$

The function  $F(t)$  will be chosen later to eliminate solutions in which  $\phi$  is a function of  $t$  alone.

Let the surface of the cross section be

$$r = a + \zeta(\theta, t), \quad (\text{A4})$$

where  $a$  is defined such that the area of the cross section is  $\pi a^2$ . The curvature of the surface is

$$\kappa = \frac{(a + \zeta)^2 + 2(\partial_\theta \zeta)^2 - (a + \zeta) \partial_{\theta\theta}^2 \zeta}{[(a + \zeta)^2 + (\partial_\theta \zeta)^2]^{3/2}}. \quad (\text{A5})$$

The kinematic condition at the surface of the cross section is

$$\left( \partial_t \zeta - \frac{1}{r^2} \partial_\theta \phi \partial_\theta \zeta + \partial_r \phi \right)_{r=a+\zeta} = 0. \quad (\text{A6})$$

The pressure at the surface of the cross section satisfies

$$p|_{r=a+\zeta} - \gamma \kappa = 0, \quad (\text{A7})$$

where  $\gamma$  is the coefficient of surface tension.

## 2. Nondimensionalization

Define dimensionless (hatted) variables

$$r = \hat{r}a, \quad \zeta = \hat{\zeta}a, \quad \kappa = \hat{\kappa}/a, \quad t = \hat{t} \left( \frac{\rho a^3}{\gamma} \right)^{1/2}, \quad (\text{A8a})$$

$$(u, v) = (\hat{u}, \hat{v}) \left( \frac{\gamma}{\rho a} \right)^{1/2}, \quad \phi = \hat{\phi} \left( \frac{\gamma a}{\rho} \right)^{1/2}, \quad p = \hat{p} \frac{\gamma}{a}. \quad (\text{A8b})$$

Writing the equations of the previous section in terms of the dimensionless variables and immediately dropping the hats, we obtain

$$\nabla^2 \phi = 0, \quad (\text{A9})$$

$$p = \partial_t \phi - \frac{1}{2} \left[ (\partial_r \phi)^2 + \frac{1}{r^2} (\partial_\theta \phi)^2 \right] + F(t), \quad (\text{A10})$$

$$\kappa = \frac{(1 + \zeta)^2 + 2(\partial_\theta \zeta)^2 - (1 + \zeta) \partial_{\theta\theta}^2 \zeta}{[(1 + \zeta)^2 + (\partial_\theta \zeta)^2]^{3/2}}, \quad (\text{A11})$$

$$\left( \partial_t \zeta - \frac{1}{r^2} \partial_\theta \phi \partial_\theta \zeta + \partial_r \phi \right)_{r=1+\zeta} = 0, \quad (\text{A12})$$

$$p|_{r=1+\zeta} - \kappa = 0. \quad (\text{A13})$$

This is the appropriate place to note that the general solution of Eq. (A9) for which the velocity is finite at the origin  $r = 0$  is

$$\phi = A_n r^n \cos n\theta, \quad (\text{A14})$$

where  $n$  is a positive integer. The factor  $\cos n\theta$  is appropriate for the symmetry of an elliptical nozzle for which  $\theta = 0$  is along one of the axes (we take this to be the major axis).

### 3. Regular perturbation expansion

Let  $\epsilon \ll 1$  be the order of magnitude of the amplitude of azimuthal mode  $n$  of the velocity potential. We now posit expansions of the variables  $\phi$ ,  $p$ ,  $\zeta$ , and  $F$  of the forms

$$\phi = \epsilon\phi_1 + \epsilon^2\phi_2 + \epsilon^3\phi_3 + O(\epsilon^4), \quad (\text{A15a})$$

$$p = 1 + \epsilon p_1 + \epsilon^2 p_2 + \epsilon^3 p_3 + O(\epsilon^4), \quad (\text{A15b})$$

$$\zeta = \epsilon\zeta_1 + \epsilon^2\zeta_2 + \epsilon^3\zeta_3 + O(\epsilon^4), \quad (\text{A15c})$$

$$F = \epsilon F_1 + \epsilon^2 F_2 + \epsilon^3 F_3 + O(\epsilon^4). \quad (\text{A15d})$$

The leading-order pressure term  $p_0 = 1$  represents the uniform capillary pressure in the cross section in the absence of motion. Anticipating, we retain the modes  $n = 2$  and  $n = 4$ , which are sufficient for representing the shape of an elliptical nozzle with a moderate ellipticity  $e$ . Let  $q$  and  $s$  be the frequencies of these two modes, respectively, replacing the notations  $\omega_2$  and  $\omega_4$  used in the main text. Then

$$q = q_0 + \epsilon q_1 + \epsilon^2 q_2 + O(\epsilon^3), \quad (\text{A16a})$$

$$s = s_0 + \epsilon s_1 + \epsilon^2 s_2 + O(\epsilon^3). \quad (\text{A16b})$$

To solve our problem we substitute the expansions (A15) into the kinematic condition (A12) and the normal stress condition (A13) and gather terms proportional to like powers of  $\epsilon$ . The resulting  $O(\epsilon)$ ,  $O(\epsilon^2)$ , and  $O(\epsilon^3)$  problems can then be solved sequentially.

### 4. $O(\epsilon)$ problem

The  $O(\epsilon)$  problem is

$$\partial_t \zeta_1 + \partial_r \phi_1|_{r=1} = 0, \quad (\text{A17})$$

$$\partial_t \phi_1|_{r=1} + \zeta_1 + \partial_{\theta\theta}^2 \zeta_1 + F_1 = 0. \quad (\text{A18})$$

Reducing Eqs. (A17) and (A18) to a single equation for  $\phi_1$ , we obtain

$$\left(\partial_{tt}^2 \phi_1 - \partial_r \phi_1 - \partial_{r\theta\theta}^3 \phi_1\right)_{r=1} + F_1' = 0. \quad (\text{A19})$$

Now we must set  $F_1'(t) = 0$  in order to avoid a purely time-dependent forcing. We thus have

$$\phi_1 = A_2 r^2 \cos 2\theta \sin qt + A_4 r^4 \cos 4\theta \sin st, \quad (\text{A20})$$

where

$$q = q_0 = \sqrt{6}, \quad s = s_0 = 2\sqrt{15}, \quad (\text{A21})$$

and  $A_2$  and  $A_4$  are dimensionless amplitudes of order unity. Equation (A17) then implies

$$\zeta_1 = \frac{2}{q} A_2 \cos 2\theta \cos qt + \frac{4}{s} A_4 \cos 4\theta \cos st. \quad (\text{A22})$$

### 5. $O(\epsilon^2)$ problem

The  $O(\epsilon^2)$  equations are

$$\begin{aligned} \partial_t \zeta_2 + \partial_r \phi_2|_{r=1} = & A_2^2 \frac{(1 - 3 \cos 4\theta) \sin 2qt}{\sqrt{6}} + 4A_4^2 \frac{(1 - 7 \cos 8\theta) \sin 2st}{2\sqrt{15}} \\ & + 4A_2 A_4 \left[ \frac{(3 \cos 2\theta - 5 \cos 6\theta) \cos st \sin qt}{2\sqrt{15}} - \frac{(3 \cos 2\theta + 5 \cos 6\theta) \cos qt \sin st}{\sqrt{6}} \right], \end{aligned} \quad (\text{A23})$$

$$\begin{aligned}
 \partial_t \phi_2|_{r=1} + \zeta_2 + \partial_{\theta\theta}^2 \zeta_2 + F_2(t) = & -2A_2 q_1 \cos 2\theta \cos qt - 2A_4 s_1 \cos 4\theta \cos st \\
 & - A_2^2 \frac{5 + 15 \cos 4\theta + (17 + 15 \cos 4\theta) \cos 2qt}{6} \\
 & - A_4^2 \frac{23 + 99 \cos 8\theta + (143 + 99 \cos 8\theta) \cos 2st}{15} \\
 & + A_2 A_4 \left[ 8 \cos 2\theta \sin qt \sin st \right. \\
 & \left. - \frac{16}{3} \left( \frac{2}{5} \right)^{1/2} (6 \cos 2\theta + 7 \cos 6\theta) \cos qt \cos st \right]. \quad (A24)
 \end{aligned}$$

In writing Eqs. (A23) and (A24) we have set  $q = q_0$  and  $s = s_0$  everywhere except in the arguments of the trigonometric functions. This introduces an  $O(\epsilon^4)$  error that is negligible for our purposes. Reducing (A23) and (A24) to a single equation for  $\phi_2$ , we obtain

$$\begin{aligned}
 (\partial_{tt}^2 \phi_2 - \partial_r \phi_2 - \partial_{r\theta\theta}^3 \phi_2)|_{r=1} + F_2'(t) = & 2\sqrt{6} A_2 q_1 \cos 2\theta \sin qt + 4\sqrt{15} A_4 s_1 \cos 4\theta \sin st \\
 & + A_2^2 \sqrt{\frac{3}{2}} (11 - 5 \cos 4\theta) \sin 2qt \\
 & + 2A_4^2 \sqrt{\frac{3}{5}} (95 - 81 \cos 8\theta) \sin 2st \\
 & + A_2 A_4 \left[ 6\sqrt{\frac{3}{5}} (25 \cos 2\theta - 7 \cos 6\theta) \cos st \sin qt \right. \\
 & \left. + 14\sqrt{6} (5 \cos 2\theta - 3 \cos 6\theta) \cos qt \sin st \right]. \quad (A25)
 \end{aligned}$$

To avoid a forcing term that depends only on time we must set  $F_2'(t) = 11(3/2)^{1/2} A_2^2 \sin 2qt + 190(3/5)^{1/2} A_4^2 \sin 2st$ , whereupon Eq. (A25) becomes

$$\begin{aligned}
 (\partial_{tt}^2 \phi_2 - \partial_r \phi_2 - \partial_{r\theta\theta}^3 \phi_2)|_{r=1} = & 2\sqrt{6} A_2 q_1 \cos 2\theta \sin qt + 4\sqrt{15} A_4 s \cos 4\theta \sin s_0 t \\
 & - 5A_2^2 \sqrt{\frac{3}{2}} \cos 4\theta \sin 2qt - 162A_4^2 \sqrt{\frac{3}{5}} \cos 8\theta \sin 2st \\
 & + A_2 A_4 \left[ 6\sqrt{\frac{3}{5}} (25 \cos 2\theta - 7 \cos 6\theta) \cos st \sin qt \right. \\
 & \left. + 14\sqrt{6} (5 \cos 2\theta - 3 \cos 6\theta) \cos qt \sin st \right]. \quad (A26)
 \end{aligned}$$

We now substitute into Eq. (A26) the general form

$$\phi_2 = r^2 \cos 2\theta G_2(t) + r^4 \cos 4\theta G_4(t) + r^6 \cos 6\theta G_6(t) + r^8 \cos 8\theta G_8(t) \quad (A27)$$

and solve the resulting equations for  $G_2$ – $G_8$ . The results are

$$G_2 = -A_2 A_4 \frac{\sqrt{5} \cos st \sin qt + 20\sqrt{2} \cos qt \sin st}{6\sqrt{3}} - A_2 q_1 \left( t \cos qt - \frac{\sin qt}{2\sqrt{6}} \right), \quad (A28)$$

$$G_4 = -\frac{5A_2^2 \sin 2qt}{12\sqrt{6}} - A_4 s_1 \left( t \cos st - \frac{\sin st}{4\sqrt{15}} \right), \quad (\text{A29})$$

$$G_6 = -7\sqrt{3}A_2A_4 \frac{22\sqrt{5} \cos st \sin qt + 65\sqrt{2} \cos qt \sin st}{1340}, \quad (\text{A30})$$

$$G_8 = -\frac{27}{44} \sqrt{\frac{3}{5}} A_4^2 \sin 2st. \quad (\text{A31})$$

Note that  $G_2$  and  $G_4$  contain secular terms  $\propto t$ . These represent unbounded resonant solutions generated by forcing terms  $\propto \cos 2\theta \sin qt$  and  $\propto \cos 4\theta \sin st$  that are solutions of the homogeneous equations. To avoid this unphysical behavior, we must set  $q_1 = s_1 = 0$ .

The final step is to determine the shape function  $\zeta_2$  by substituting Eq. (A27) into Eqs. (A23) and (A24). We also require the (dimensionless) area of the cross section to be  $\pi$ , viz.,

$$\int_0^{2\pi} d\theta \int_0^{1+\zeta} r dr = \int_0^{2\pi} \frac{1}{2} (1 + \zeta)^2 d\theta = \pi. \quad (\text{A32})$$

The result is

$$\begin{aligned} \zeta_2 = & \frac{A_2^2}{36} [3(2 \cos 4\theta - 1) + (4 \cos 4\theta - 3) \cos 2qt] \\ & + \frac{A_4^2}{2310} [11(22 \cos 8\theta - 7) - 7(4 \cos 8\theta + 11) \cos 2st] \\ & + \frac{A_2 A_4}{6030} \cos 2\theta [5(378 \cos 4\theta - 55) \sin qt \sin st \\ & + \sqrt{10}(1752 \cos 4\theta - 1747) \cos qt \cos st]. \end{aligned} \quad (\text{A33})$$

## 6. $O(\epsilon^3)$ problem

The  $O(\epsilon^3)$  problem serves to determine the  $O(\epsilon^2)$  frequency coefficients  $q_2$  and  $s_2$ . In the interest of brevity, we proceed directly to the equation satisfied by  $\phi_3(r, \theta, t)$ , which is

$$\begin{aligned} & (\partial_{tt}^2 \phi_3 - \partial_r \phi_3 - \partial_{r\theta\theta}^3 \phi_3) \Big|_{r=1} \\ & = \cos 2\theta \left[ \left( \frac{11}{12} A_2^3 + \frac{411877}{7035} A_2 A_4^2 + 2\sqrt{6} A_2 q_2 + \frac{21}{4} A_2^3 \cos 4\theta \right. \right. \\ & \quad \left. \left. - \frac{229493}{2345} A_2 A_4^2 \cos 4\theta + \frac{49104}{335} A_2 A_4^2 \cos 8\theta \right) \sin qt \right. \\ & \quad \left. + \frac{5}{3} A_2^3 \sin 3qt - \frac{A_2 A_4^2}{402} (4361\sqrt{5/2} \cos qt \sin 2st + 77689 \sin qt \cos 2st) \right] \\ & + \cos 4\theta \left[ \left( \frac{19325}{402} A_2^2 A_4 - \frac{45159}{385} A_4^3 + 4\sqrt{15} A_4 s_2 + \frac{25974}{55} A_4^3 \cos 8\theta \right) \sin st \right. \\ & \quad \left. - \frac{1140}{11} A_4^3 \sin 3st - \frac{2682}{67} A_2 A_4 \cos 2qt \sin st \right. \\ & \quad \left. - \frac{6053}{134} \sqrt{5/2} A_2^2 A_4^2 \sin 2qt \cos st \right] + (\dots) \cos 6\theta \\ & + (\dots) \cos 8\theta + (\dots) \cos 10\theta + (\dots) \cos 12\theta, \end{aligned} \quad (\text{A34})$$

where ellipses indicate terms we do not care about. The solution of Eq. (A34) has the general form

$$\phi_3 = \sum_{m=1}^6 r^{2m} \cos 2m\theta H_{2m}(t). \quad (\text{A35})$$

Now substitute Eq. (A35) into Eq. (A34), multiply by  $\cos 2\theta$ , and apply  $\int_0^{2\pi} d\theta$  to the result to obtain a second-order differential equation for  $H_2(t)$ . Multiplying by  $\cos 4\theta$  and integrating gives a similar equation for  $H_4(t)$ . The solutions are

$$H_2(t) = -\left(\frac{37}{12\sqrt{6}}A_2^3 + \frac{3865}{804\sqrt{6}}A_2A_4^2 + A_2q_2\right)t \cos qt + \text{periodic terms}, \quad (\text{A36a})$$

$$H_4(t) = -\left(\frac{3865\sqrt{15}}{4824}A_2^2A_4 + \frac{305\sqrt{15}}{154}A_4^3 + A_4s_2\right)t \cos st + \text{periodic terms}, \quad (\text{A36b})$$

where the periodic terms involve multiples, sums, and differences of the wavenumbers  $q$  and  $s$ . Both  $H_2(t)$  and  $H_4(t)$  contain unbounded resonant terms proportional to  $t$ . These unphysical terms must vanish, which implies

$$q_2 = -\frac{37}{12\sqrt{6}}A_2^2 - \frac{3865}{804\sqrt{6}}A_4^2 \rightarrow q = \sqrt{6}\left[1 - \epsilon^2\left(\frac{37}{72}A_2^2 + \frac{3865}{4824}A_4^2\right)\right], \quad (\text{A37a})$$

$$s_2 = -\frac{305\sqrt{15}}{154}A_4^2 - \frac{3865\sqrt{15}}{4824}A_2^2 \rightarrow s = 2\sqrt{15}\left[1 - \epsilon^2\left(\frac{305}{308}A_4^2 + \frac{3865}{9648}A_2^2\right)\right]. \quad (\text{A37b})$$

The final step is to rewrite the foregoing expressions in terms of the (dimensional) amplitudes  $b_2 = 2\epsilon a A_2/\sqrt{6}$  and  $b_4 = 2\epsilon a A_4/\sqrt{15}$ . The resulting expressions for the jet radius  $R$  and the frequencies  $q \equiv \omega_2$  and  $s \equiv \omega_4$  are then Eqs. (20)–(22) in the main text. Those expressions agree with the results of Bohr [5] in the single-mode limits  $b_2 = 0$  and  $b_4 = 0$ .

### 7. Critical amplitude $b_{2\text{crit}}$

Figure 6 shows that the shape of a cross section of the jet becomes reentrant when the amplitude  $b_2$  exceeds a critical value  $b_{2\text{crit}}$ . If only the  $n = 2$  mode is present ( $b_4 = 0$ ), then expression (20) for the jet's radius reduces to Eq. (11a). The critical value  $b_{2\text{crit}}$  is a minimum for  $t = 0$ , at which point the jet's radius is

$$R(\theta, 0) = a + b_2 \cos 2\theta + \frac{b_2^2}{12a}(5 \cos 4\theta - 3) \equiv f(\theta). \quad (\text{A38})$$

The critical azimuth of reentry occurs at a value of  $\theta$  such that  $dy/d\theta \equiv d(R \sin \theta)/d\theta = 0$ , or  $f \cos \theta + f' \sin \theta = 0$ . This implies

$$12 + \hat{b}_2(-24 + 17\hat{b}_2) + 4(9 - 10\hat{b}_2)\hat{b}_2 \cos 2\theta + 25\hat{b}_2^2 \cos 4\theta = 0, \quad (\text{A39})$$

where  $\hat{b}_2 = b_2/a$ . Equation (A39) has the solution

$$\cos 2\theta = \frac{-9\hat{b}_2 + 10\hat{b}_2^2 \pm \hat{b}_2 \sqrt{200\hat{b}_2^2 + 120\hat{b}_2 - 69}}{25\hat{b}_2^2}. \quad (\text{A40})$$

The critical value of  $\hat{b}_2$  corresponds to the vanishing of the discriminant in Eq. (A40). Of the two solutions, the relevant one is

$$b_{2\text{crit}} = \frac{\sqrt{174} - 6}{20}a \approx 0.3595a. \quad (\text{A41})$$



- [1] L. Rayleigh, On the instability of jets, *Proc. London Math. Soc.* **s1-10**, 4 (1878).
- [2] L. Rayleigh, On the capillary phenomena of jets, *Proc. R. Soc. London* **29A**, 71 (1879).
- [3] G. Bidone, Expériences sur la forme et sur la direction des veines et des courans d'eau lancés par diverses ouvertures, *Mem. Acad. Sci. Torino* **34**, 229 (1830).
- [4] H. von Buff, Einige Bemerkungen über die Erscheinung der Auflösung des flüssigen Strahls in Tropfen, *Justus Liebigs Ann. Chem.* **78**, 162 (1851).
- [5] N. Bohr, Determination of the surface-tension of water by the method of jet vibration, *Philos. Trans. R. Soc. A* **209**, 281 (1909).
- [6] J. F. Geer and J. C. Strikwerda, Vertical slender jets with surface tension, *J. Fluid Mech.* **135**, 155 (1983).
- [7] S. E. Bechtel, The oscillation of slender elliptical inviscid and Newtonian jets: Effects of surface tension, inertia, viscosity and gravity, *Trans. ASME* **56**, 968 (1989).
- [8] T. V. Kasyap, D. Sivakumar, and B. N. Raghunandan, Breakup of liquid jets emanating from elliptical orifices at low flow conditions, *Atomization Sprays* **18**, 645 (2008).
- [9] T. V. Kasyap, D. Sivakumar, and B. N. Raghunandan, Flow and breakup characteristics of elliptical liquid jets, *Int. J. Multiphase Flow* **35**, 8 (2009).
- [10] G. Amini and A. Dolatabadi, Axis-switching and breakup of low-speed elliptic liquid jets, *Int. J. Multiphase Flow* **42**, 96 (2012).
- [11] S. Gu, L. Wang, and D. L. S. Hung, Instability evolution of the viscous elliptic liquid jet in the Rayleigh regime, *Phys. Rev. E* **95**, 063112 (2017).
- [12] E. Farvardin and A. Dolatabadi, Numerical simulation of breakup of elliptical liquid jet in still air, in *Proceedings of the ASME 2012 Fluids Engineering Summer Meeting 2012*, pp. 1–5 (unpublished).
- [13] M. R. Morad, M. Nasiri, and G. Amini, Numerical modeling of instability and breakup of elliptical liquid jets, *AIAA J.* **58**, 2442 (2020).
- [14] N. Chen and H. Yu, Mechanism of axis switching in low aspect-ratio rectangular jets, *Comput. Math. Appl.* **67**, 437 (2014).
- [15] C. K. Muthukumaran and A. Vaidyanathan, Experimental study of elliptical jet from sub to supercritical conditions, *Phys. Fluids* **26**, 044104 (2014).
- [16] K. R. Rajesh, R. Sakthikumar, and D. Sivakumar, Interfacial oscillation of liquid jets discharging from non-circular orifices, *Int. J. Multiphase Flow* **87**, 1 (2016).
- [17] S. Moon, Y. Shin, H. Kwak, J. Yang, S.-B. Lee, S. Kim, and K. An, Experimental observations of Bohr's nonlinear fluidic surface oscillation, *Sci. Rep.* **6**, 19805 (2016).
- [18] A. Jaberri and M. Tadjfar, Wavelength and frequency of axis-switching phenomenon formed over rectangular and elliptical liquid jets, *Int. J. Multiphase Flow* **119**, 144 (2019).
- [19] A. Jaberri and M. Tadjfar, Comparative study on interfacial oscillations of rectangular and elliptical liquid jets, *Proc. Inst. Mech. Eng. Part G* **234**, 1272 (2020).
- [20] Y. Y. Ma and D. Z. Zhu, Axis switching of free-falling elliptical water jets, *J. Hydraul. Eng.* **146**, 06020009 (2020).
- [21] J. W. M. Bush and A. E. Hasha, On the collision of laminar jets: Fluid chains and fishbones, *J. Fluid Mech.* **511**, 285 (2004).
- [22] E. J. Gutmark and F. F. Grinstein, Flow control with noncircular jets, *Annu. Rev. Fluid Mech.* **31**, 239 (1999).
- [23] A. P. S. Wheeler, S. Morad, N. Buchholz, and M. M. Knight, The shape of the urine stream—from biophysics to diagnostics, *PLoS One* **7**, 1 (2012).
- [24] J. M. Berghorson, K. Sone, T. W. Mattner, P. E. Dimotakis, D. G. Goodwin, and D. I. Meiron, Impinging laminar jets at moderate Reynolds numbers and separation distances, *Phys. Rev. E* **72**, 066307 (2005).
- [25] See Supplemental Material at <http://link.aps.org/supplemental/10.1103/PhysRevFluids.7.104001> for experimental details and additional results.
- [26] S. Popinet, Gerris: A tree-based adaptive solver for the incompressible Euler equations in complex geometries, *J. Comput. Phys.* **190**, 572 (2003).